drones

MDPI

Article

Electric and Magnetic Fields Analysis of the Safety Distance for UAV Inspection around Extra-High Voltage Transmission Lines

Issam Boukabou * and Naima Kaabouch

School of Electrical Engineering and Computer Science, University of North Dakota, Grand Forks, ND 58202, USA; naima.kaabouch@und.edu
* Correspondence: issam.boukabou@und.edu

Abstract: The deployment of small unmanned aerial vehicles (UAVs), or drones, for transmission line inspections, has brought attention to the potential impact of electromagnetic fields (EMFs) on UAV operations. This work describes a mathematical model based on the finite elements method (FEM), designed to examine the electric and magnetic fields produced by extra-high voltage (EHV) conductors. The current study extends the analysis to encompass both electric and magnetic fields and evaluates the safe distances for UAVs operating near 345 kV, 500 kV, and 765 kV transmission lines. The electromagnetic environment around these EHV transmission lines was simulated using electrostatic, magnetostatic, and transient magnetic modules within the QuickField software 6.6. Electric and magnetic profiles were estimated using 2D finite element analysis, including a numerical simulation for phase-to-phase fault EMFs for the above transmission lines. These results were then cross-verified with theoretical calculations at specific intervals and further validated using the EMFACDC analytical method developed by the International Telecommunication Union. This comprehensive assessment concludes that precise distance considerations are necessary to ensure UAV safety during power line inspections, mitigating potential risks from EMF interference.

Keywords: electric field; magnetic field; EMF; extra-high voltage; finite element method; QuickField software; safe distance; transient magnetic; power lines; transmission lines; UAV; UAS

Citation: Boukabou, I.; Kaabouch, N. Electric and Magnetic Fields Analysis of the Safety Distance for UAV Inspection around Extra-High Voltage Transmission Lines. *Drones* **2024**, *8*, 47. https://doi.org/10.3390/drones8020047

Academic Editor: Abdessattar Abdelkefi

Received: 28 November 2023
Revised: 19 January 2024
Accepted: 25 January 2024
Published: 2 February 2024

1. Introduction

Unmanned aerial vehicles (UAVs) are becoming indispensable tools for power line inspections. Their unmatched maneuverability, ability to access hard-to-reach locations, and reduced risks to human inspectors position them as superior alternatives to traditional inspection methods. However, the electromagnetic fields (EMFs) generated by power lines present a significant challenge, interfering with UAV flight stability, navigational systems, and payload functionality. This interference is further accentuated as most modern UAVs comprise non-metallic materials like carbon-fiber composites, which make them susceptible to electromagnetic interference (EMI).

Over the last decade, significant research has been conducted to understand and mitigate the effects of EMFs on UAVs during power line inspections. For instance, the authors of [1] highlighted the varying susceptibilities to EMI among different UAV brands and models. They concluded that the onboard sensor package is the most susceptible to EMI compared to other parts of the UAV. In [2], the authors showed that electric fields above 50 kV/m led to UAV instability, suggesting a threshold for stable UAV operation. The study also highlighted the qualitative effects of EMFs on UAVs, pointing to the need for quantitative data for safety measures. Additionally, they showed that magnetic fields over 180 μT made UAVs drift towards power lines, affecting the magnetometer function. However, the research did not address the response of different UAV models to these disturbances or their operational implications. Furthermore, the United States Department of Homeland Security cited a similar threshold of 50 kV/m [3] for modeling infrastructure

resilience against electromagnetic pulses. In [4], a study on small UAVs in the electric utility industry reported EMI disruptions within 2–4 m of active equipment but none beyond 10 m. It highlighted that various UAVs, sensors, and infrastructure combinations can show distinct EMF behaviors affecting missions. However, this study did not specify the type of sensor susceptible to EMI interference or the movement of the UAV during the inspection. In [5], the authors simulated the effects of EMFs from a 500 kV tower on UAVs. They found significant electric field changes, with UAVs withstanding up to 300 kV/m before failure. Based on their simulations, they concluded that for a distance of 4.5 m or above, the UAV flight control system can be considered to work normally. In [6], the authors assessed EMI on UAVs during inspections of 345 kV and 765 kV power lines in South Korea. Their tests revealed interference within 15 m for 345 kV lines and 30 m for 765 kV lines. Therefore, they set 30 m and 45 m safety distances, respectively, to avoid GPS and sensor disruptions.

Various methods have been proposed to predict, model, and mitigate the interference from EMFs in UAVs. For instance, [7] modeled the electromagnetic field around power transmission lines, considering the position, electric current, and tower topology. They used Biot–Savart and Ampere's laws to simulate and test the model with a quadrotor near 230 kV towers. Their results showed that the predicted interference closely matched real-world interference. The authors in [8] described a method to counteract EMI on UAVs from power structures. The UAV was more stable near transmission lines when the Biot–Savart equations were used in an extended Kalman filter. The simulations showed deviations without this filter, and in real-world tests at a hydroelectric facility, the filter-equipped UAV effectively navigated around high-voltage equipment.

However, there is a need for standardized methodologies and metrics across these studies for assessing the interference on UAVs, making it challenging to compare results and derive universally applicable conclusions and recommendations. Nonetheless, collectively, these studies underscore the urgent need for a comprehensive understanding and modeling EMFs around power lines. They also highlight the necessity for clear guidelines on safe operational distances for UAVs during power line inspections. In addition, empirical data that could establish a safe distance for UAV inspections of transmission lines needs to be included. Safety distances are largely based on the subjective judgment and experience of operators, who aim to prevent accidents such as collisions, loss of control, or the UAV getting too close to the tower or transmission lines. Although operators utilize ground control stations and remote controls to control UAVs during power line inspections remotely, this approach needs to fully leverage UAVs' agility and efficiency.

While some studies recommend precise, safe distances, these are often impractical for UAV inspections that require proximity for high-resolution imagery and infrastructure examination. Overly conservative distance recommendations can undermine the effectiveness of the inspections. For example, maintaining a distance of 10 m, as recommended by [4], may prevent a UAV from inspecting the underside of a power line tower. However, if safe operation is feasible at 5 m, the UAV can collect crucial data to assess the tower's condition. Therefore, there is a clear need for a more refined understanding of safe distances tailored to specific transmission line environments and further research to determine a safe distance for UAV inspections. This underscores the significance of this research.

Various computational techniques, including the surface charge simulation method, charge simulation technique, Monte Carlo method, and finite difference method, have traditionally been used for calculating electric and magnetic fields. In this study, the finite element method (FEM) is employed. FEM sets itself apart with its exceptional ability to manage complex problems. These challenges often involve nonlinear characteristics, time variations, and, particularly pertinent to our study, the circular geometries of high-voltage conductors [9]. The choice of FEM, especially when considering thin wire applications, required careful validation to ensure its accuracy. To this end, our FEM results were compared with an analytical method. This comparison yielded a high degree of correlation, significantly reinforcing our confidence in FEM's applicability to the study of electric and magnetic fields around thin wires. In addition to the robustness of FEM in handling com-

plex geometrical and physical phenomena, QuickField software emerged as an equally crucial tool in our research. Its ease of use and capabilities for rapid prototyping and iterative analysis made it highly suitable for our research. QuickField's efficiency is particularly advantageous given the extensive number of simulations required in our study. Moreover, its versatility and seamless integration into standard programs further enhanced its applicability to our research goals.

This paper, an extended work of [10,11], describes the design and development of a robust simulation environment for assessing safe distances during UAV inspections of extra-high voltage (EHV) transmission lines under both normal and transient operating conditions. The simulation environment accounts for various UAV operational conditions and power line configurations. The developed system uses the QuickField software package, offering high fidelity in modeling the electric and magnetic fields around transmission lines. The identified safe operational distances will enhance the safety and efficiency of UAVs during power line inspections.

The paper is structured as follows: Section 2 describes the construction of the model, explaining the procedures and methods used to simulate electric and magnetic fields around various transmission line profiles using QuickField software. Section 3 presents and compares the simulation results with the results of an analytical method-based simulation software. Finally, Section 4 concludes the findings and provides insights into future research directions.

2. Materials and Methods

This section describes the model configuration, the analytical framework, and the FEM technique used in this study. The transmission lines considered in this study have standard tower dimensions.

2.1. Model Description

This investigation considered three-phase EHV power lines with shield wires at voltages of 345 kV, 500 kV, and 765 kV, as depicted in Figure 1. The 345 kV line consists of two identical three-phase circuits, each with two conductors per phase. The phase conductors were of type 636 CAA-26/7 MCM, each with an area of 240 mm^2. The shield wires (SW1 and SW2) were composed of seven-wire Harmonized System galvanized steel. In contrast, the 500 kV and 765 kV lines had a single horizontal circuit with two conductors per phase spaced 32.2 mm apart and four conductors per phase spaced 32.0 mm apart, respectively. The phase conductors were of type 795 MCM. Furthermore, the shield wires (SW1 and SW2) were made of nine-wire HS galvanized steel [12,13]. Shield wires are primarily designed for lightning protection and are grounded. They can have a shielding effect on electric fields due to their placement and grounding, which can lead to a minimal redistribution of the electric field lines. Since shield wires typically do not carry operational currents under normal conditions, they would have little to no impact on the magnetic field profiles around the live conductors unless they carry fault currents during lightning strikes or fault conditions. In such cases, they could temporarily affect the magnetic field distribution due to the sudden surge of current [14].

Table 1 lists the characteristics of each power line, including the voltage, current, and conductor configuration. The most common 345 kV conductor configuration, termed "Untransposed", was used for this work.

Table 1. Input data of the EHV transmission lines [15].

Nominal Voltage Level [kV]	345	500	765
Highest system current rating at 80 °C [kA]	1.29	2.58	4.16
Frequency [Hz]	60	60	60

Table 1. *Cont.*

Nominal Voltage Level [kV]	345	500	765
Phase angle [deg.]	C-C: 0–240 B-B: 120–120 A-A: 240–0	A: 0 B: 120 C: 240	A: 0 B: 120 C: 240
Distance between phases and ground [m]	C-C: 5.95 B-B: 7.5 A-A: 5.95	24.48	54
Nominal cross-section [mm^2]	Bundle	Bundle	Bundle
	2 × 240	2 × 560	4 × 560
Equivalent radius [mm]	21.9	26	32.2

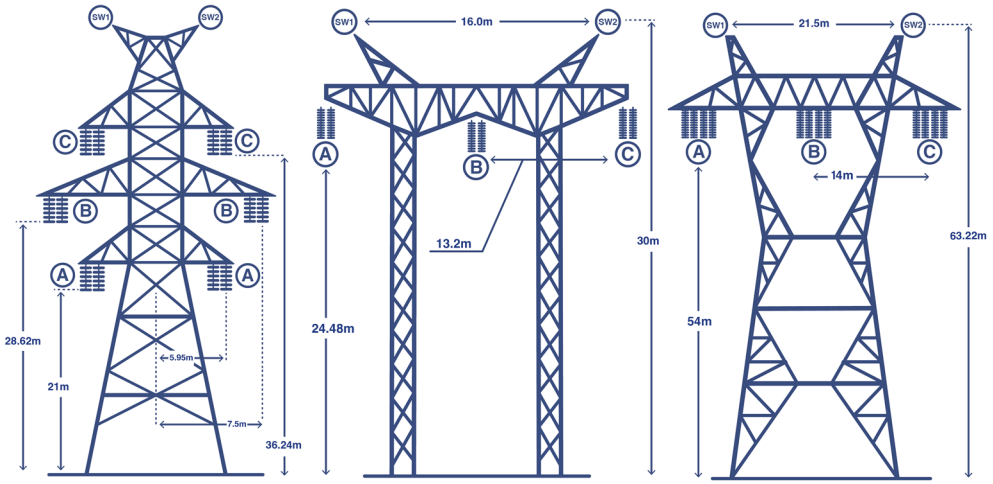

Figure 1. Standard dimensions for 345 kV, 500 kV, and 765 kV power lines [10].

In this study, the line sources are aligned with the *z*-axis of the Cartesian coordinate system, with the origin positioned between phases B for the double-circuit configuration and directly on phase B for the single-circuit configuration. Figure 2 illustrates the positioning and orientation of the selected coordinate system for both the double- and single-circuit configurations.

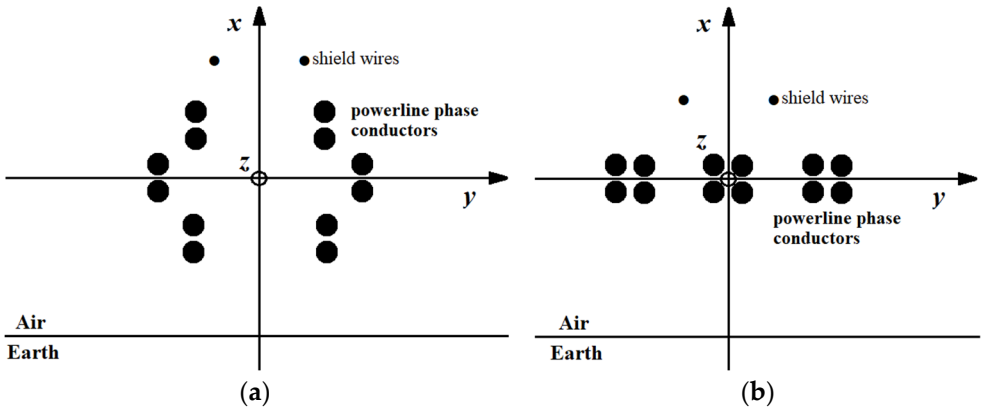

Figure 2. Analytical graphical position of the selected coordinate system for: (**a**) double-circuit configuration; (**b**) single-circuit configuration.

2.2. Electric Field and Magnetic Vector Potential Formulation

The mutual relationship and properties of electric fields and magnetic fields can be described using Maxwell's four basic equations [16]. These equations are based on Ampere's law, Faraday's law of induction, Gauss' law, and Gauss' law for magnetism.

$$\nabla \times \overline{E} = -\frac{\partial \overline{B}}{\partial t} \tag{1}$$

$$\nabla \times \overline{H} = \overline{J} + \frac{\partial \overline{D}}{\partial t} \tag{2}$$

$$\nabla . \overline{D} = \rho \tag{3}$$

$$\nabla . \overline{B} = 0 \tag{4}$$

where $\overline{E}$, $\overline{H}$, $\overline{J}$, $\overline{D}$, $\overline{B}$, and ρ are the electric field strength, magnetic field strength, current density, dielectric flux density, magnetic flux density, and electric charge density, respectively.

To extend these fundamental principles, we introduce the electric field potential V and magnetic vector potential A:

$$\overline{E} = -\nabla V \tag{5}$$

$$\overline{B} = \nabla \times \overline{A} \tag{6}$$

The electric potential V and magnetic vector potential A in any region depends on the coordinates (x, y, z) and their derivatives. In our study, we considered only a 2D plane, hence focusing on the (x, y) coordinates.

2.3. FEM Analysis for the Electric Field Problem

FEM is founded on the principle that physical systems stabilize at minimum energy levels. When applied to electric field calculations, the FEM-solving process begins with dividing the solution region into finite-number subregions, known as region discretization. Each subregion or element is then analyzed, and an equation is developed. The next step is element assemblage, which involves assembling all equations from each subregion. In our problem, FEM aims to determine the electric scalar potential function V that minimizes the energy functional as follows:

$$F(V) = \int_D \left(\frac{1}{2} \varepsilon |\nabla V|^2 - \rho_v V \right) \mathrm{dD} \tag{7}$$

where D represents the volume of the region under consideration, ε is the permittivity of the material, ρ_v is the volume charge density, and ∇V is the gradient of the electric potential. The integral over D calculates the total electrostatic energy stored in the field and the work carried out against the electric forces within the volume. The functional reaches its stationary value when:

$$\delta F(V) = \int_D (\varepsilon \nabla V . \nabla \delta V - \rho_v \delta V) \mathrm{d}D = 0 \tag{8}$$

this equation establishes the necessary conditions for the minimization of the functional, leading to Poisson's equation in regions with charge and Laplace's equation in charge-free zones. In 2D Cartesian coordinates (x, y), the functional for the electrostatic field is expressed as follows:

$$F(V) = \int_D \left(\frac{1}{2} \varepsilon \left(\left(\frac{\partial V}{\partial x} \right)^2 + \left(\frac{\partial V}{\partial y} \right)^2 \right) - \rho_v V \right) \mathrm{d}D \tag{9}$$

where region D is discretized into numerous small elements, forming a mesh with nodes. The potential function V is then approximated by a sum of shape functions $f_j(r)$ associated with each node j [9]:

$$V(r) = \sum_{j=1}^{n} V_j f_j(r) \tag{10}$$

where V_j is the electric potential at node j, and r is any point within the region D. Substituting this approximation into the energy functional, we obtain an approximate form W^*, which is minimized under the following conditions:

$$\frac{\partial W^*}{\partial V_j} = 0 \quad \text{for } j = 1,\ 2,\ ...,\ n \tag{11}$$

this results in a system of equations, with the unknowns being the electric potential values at the mesh nodes [17]. Solving this system yields the electric field distribution within the region based on the gradient of the potential established in Equation (10).

$$E_m = (-\nabla V)_m = -\sum_{j=1}^{n} V_j f_j^m \tag{12}$$

2.4. FEM Analysis for the Magnetic Field Problem

Similar to the electric field calculations, stabilizing the physical systems through magnetic field calculations involves determining a magnetic vector potential function A that minimizes the functional:

$$\int_D \left(\frac{1}{2}\mu|\nabla \times A|^2 - J.A\right) dD + \int_{\sum_N} f_N A.\mathrm{d}S \tag{13}$$

where D is the volume of the proposed region, μ is the magnetic permeability, J represents the current density within volume D, $\sum_N$ is the boundary surface with Neumann conditions, and f_N is the function defined by these conditions. The surface integral accounts for the boundary conditions on the magnetic vector potential. The necessary conditions for the stationarity of this function is

$$\delta F(A) = \int_D (\mu(\nabla \times A).(\nabla \times \delta A) - J.\delta A)\mathrm{d}D + \int_{\sum_N} f_N \delta A.\mathrm{d}S = 0 \tag{14}$$

In Cartesian coordinates $(x,\ y)$, the energy functional's expression is

$$F(A) = \int_D \left(\frac{1}{2}\mu\left(|\nabla \times A|^2\right) - J.A\right)\mathrm{d}D \tag{15}$$

The magnetic vector potential A is then approximated as follows:

$$A(r) = \sum_{j=1}^{n} A_j f_j(r) \tag{16}$$

where A_j is the magnetic vector potential at node j, r is any point in the proposed region, and $f_j(r)$ is the shape function, unique to each node j.

Substituting this approximation into the energy functional, the approximate energy W^* is obtained and minimized under the following conditions:

$$\frac{\partial W^*}{\partial A_j} = 0 \quad \text{for } j = 1,\ 2,\ ...,\ n \tag{17}$$

The magnetic field intensity within each element can be determined using the curl of the magnetic vector potential A, expressed as follows:

$$B_m = \nabla \times A_m = \sum_{j=1}^{n} \nabla \times \left(A_j f_j^m\right) \tag{18}$$

Similar to the electric case, the estimated magnetic field intensity within each finite element closely mirrors the actual field distribution, offering a precise and comprehensive understanding of the magnetic field behaviors.

2.5. QuickFiekd Simulation Model Procedures

To calculate the EMF, QuickField is used, which is a finite element analysis software package for electromagnetic, stress, and thermal analysis [18]. This software solves Maxwell's equations to calculate EMFs near transmission lines. It represents the problem as a set of smaller parts, commonly called finite elements. These elements are known for their simple structure compared to the original system.

All Quickfield simulations and EMFACDC model in this work were performed assuming that each transmission line sub-conductor was modeled by replacing each conductor bundle with an equivalent conductor of radius r_{eq}, as given in [19].

$$r_{eq} = \sqrt[n]{nrA^{(n-1)}} \tag{19}$$

where n is the number of sub-conductors, r is the radius of the sub-conductor, and A is the bundle radius. The influence of the dimensions of a conductor, mainly when dealing with multiple conductors, can be assessed by using the equivalent conductor diameter provided by Equation (11). Essentially, this diameter is that of a hypothetical single conductor, which would carry the same amount of electric charge per unit length as the bundle, resulting in a comparable electric field. The study referenced in [16] provides evidence that modeling individual and bundled conductors yields equivalent results, assuming perfect symmetry in the physical arrangement. However, this assumption typically holds under the ideal conditions assumed in this work. Factors such as conductor sag, tension variations, and non-uniform current distribution can cause discrepancies between the two modeling approaches.

Figure 3 shows the procedure used in simulating the electric and magnetic fields. The process starts with defining the model geometry along with the boundary conditions. Physical properties like ground, voltage (amplitude and phase), and air for each line conductor are entered into the model. Mesh generation is carried out to discretize the model, and various simulation conditions are explored. The obtained results are then compared to analytical methods and exported as text for easy data manipulation.

For this simulation, the transmission line conductors were assumed to be infinitely long, straight, parallel to the ground, and parallel to each other. Each active conductor was modeled as a simple copper cylinder with an electrical conductivity of 6 S/m. For the electrostatic model, the electric potential at ground level and the semicircular boundary were set to zero ($U = 0$). For the magnetostatic model, the transmission line was positioned above ground with a magnetic permeability of 1 and a soil electrical conductivity of 0.02 S/m. A half-balloon type boundary condition ($R = 320$ m) was implemented, as shown in Figure 4, which simulates space that extends infinitely [9]. For each power line simulation, over a half-million mesh elements were required to achieve good symmetry and satisfactory analysis.

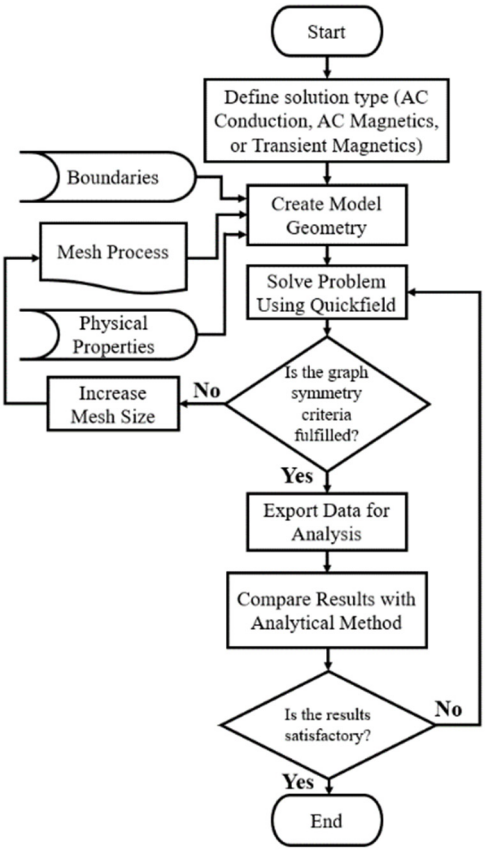

Figure 3. Flow chart for the EMF simulation procedure.

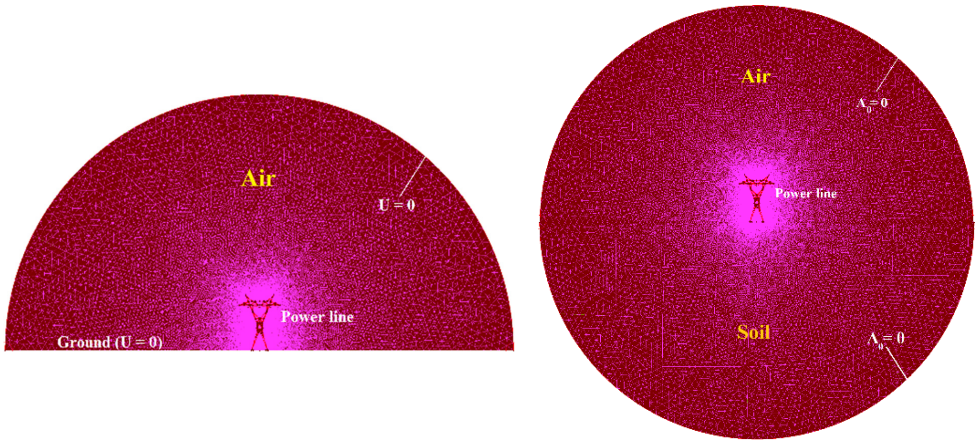

(**a**) (**b**)

Figure 4. Discretized global FEM for (**a**) electrostatic model of the single-circuit transmission line showing the boundary region; (**b**) magnetostatic model of the single-circuit transmission line showing the boundary region.

3. Results and Discussion

The EMFs were calculated for three types of flights: vertical (y), horizontal (x), and circular (R), as shown in Figure 5. Figure 5a shows the UAV moving in the x- or y-direction, and Figure 5b shows the UAV moving around the transmission line at a fixed radius R.

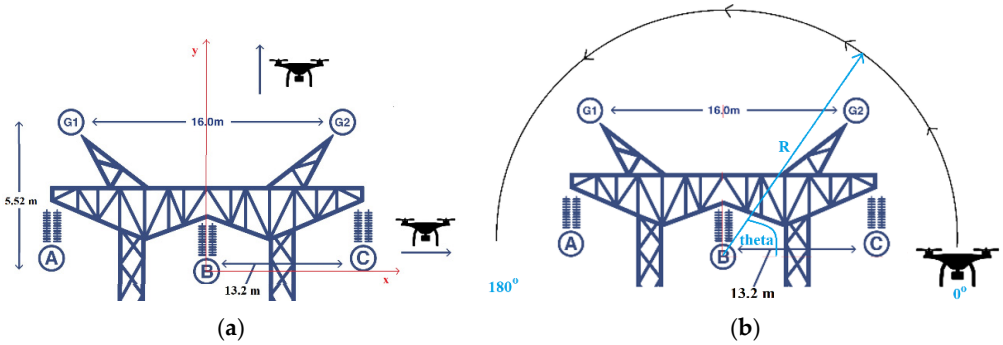

(**a**) (**b**)

Figure 5. Direction of motion for (**a**) x, y scenario; (**b**) radius scenario.

3.1. Electric Field

Simulation results are illustrated in Figure 6. Figure 6a,b depict the electric field as a function of distance from the power line conductors in the x- and y-directions, respectively, for the three power line types. As expected, the electric field is very high around the phase conductors and decreases exponentially as the UAV moves away from the power lines. Due to the geometry of the 345 kV power line, the electric field increases at 5 m, reaching a maximum at 7.5 m, followed by a sharp drop.

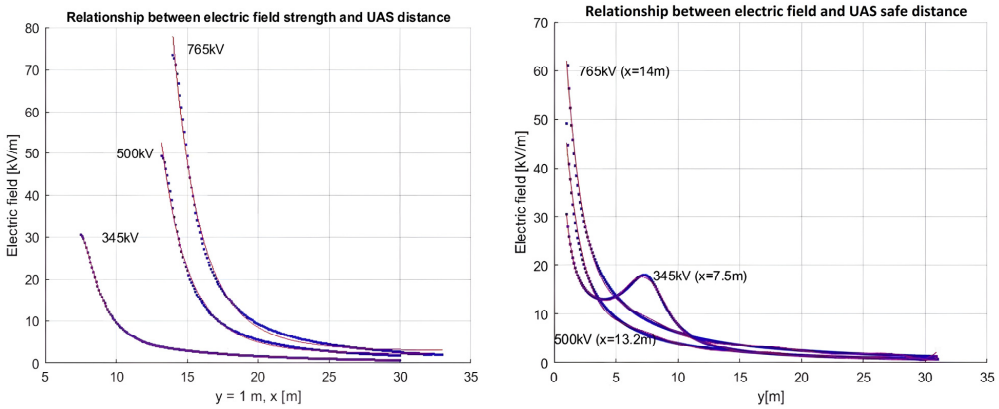

(**a**) (**b**)

Figure 6. Electric field as a function of (**a**) horizontal movement; (**b**) vertical movement.

Figure 7 shows the distribution of the electric fields at different heights for horizontal movement above and below the centerline of phase B in the double-circuit configuration and for the three phases in the single-circuit configuration. As expected, the electric field reaches its maximum at the horizontal coordinates of the phases and decreases as the UAV moves vertically away from the power lines. For instance, at a vertical distance of ± 1 m, the electric field strength peaked at 30.2 kV/m, 50.6 kV/m, and 78.5 kV/m for transmission lines of 345 kV, 500 kV, and 765 kV, respectively. However, at a vertical distance of y = ± 10 m, the peak electric field strength decreases to 0.6 kV/m, 3.6 kV/m, and 5.6 kV/m, respectively.

Figure 8 presents a three-dimensional map of the electric field strength for the three power line types. The electric field is concentrated around the phase conductors and gradually decreases as the UAV moves away from them. An extra degree of cancellation can be observed in the electric field generated by the 345 kV transmission line between the fields of the individual conductors.

Figure 9 shows the electric field intensity for four different radii for each of the power line types. The UAV movement began on the right side of the transmission line and ended on the left. For each figure, the left side of the plots corresponds to an angle of 0°, and the right side corresponds to 180°. For these two angles, the electric field values are higher

for the 500 kV and 765 kV power lines. For the 345 kV power line, the electric field has two maxima at 40° and 140° and a minimum at about 90°. In general, the electric field decreases as the radius increases. For circular flights, the highest field values correspond to an approximate radius of 15 m due to the shape of the towers.

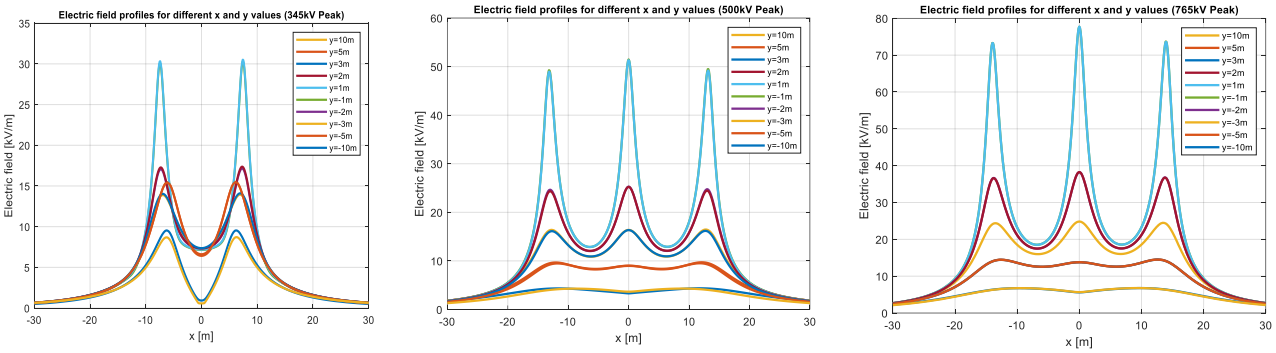

(**a**) (**b**) (**c**)

Figure 7. Lateral profiles of electric fields for heights between -10 and +10 m for the three power line voltages: (**a**) 345 kV, (**b**) 500 kV, and (**c**) 765 kV.

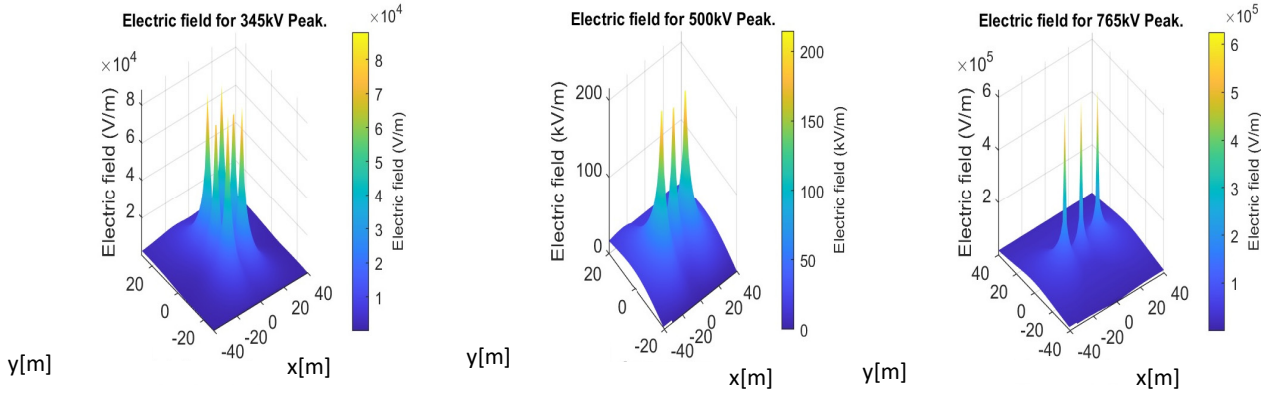

(**a**) (**b**) (**c**)

Figure 8. Three-dimensional plots of the electric field for the three power line voltages: (**a**) 345 kV, (**b**) 500 kV, and (**c**) 765 kV.

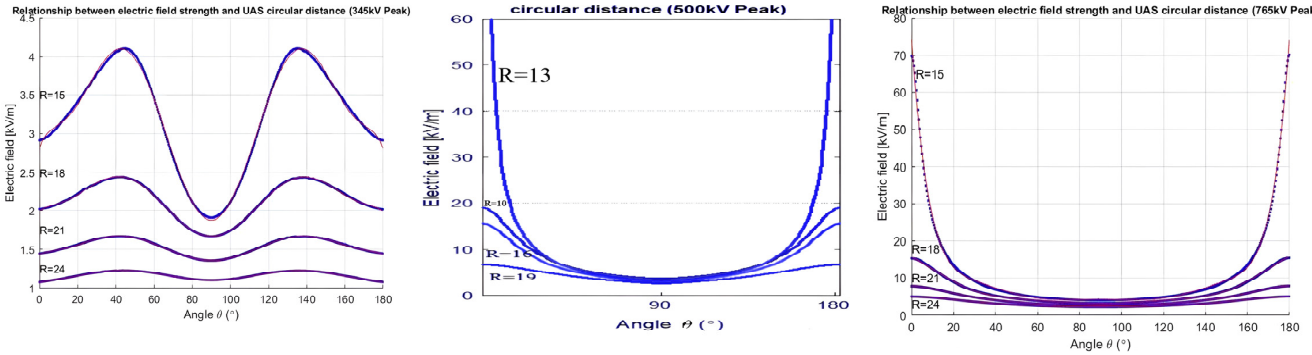

(**a**) (**b**) (**c**)

Figure 9. Electric field for different angles and radii for the three power line voltages: (**a**) 345 kV, (**b**) 500 kV, and (**c**) 765 kV.

3.2. Magnetic Field

The simulation results are illustrated in Figure 10. Figure 10a,b depicts the resultant magnetic field as a function of distance from the power line conductors in the *x*- and *y*-directions, respectively, for each of the three power line types. These figures have similar profiles as the electric fields shown in Figure 6, but the magnetic field values are much higher.

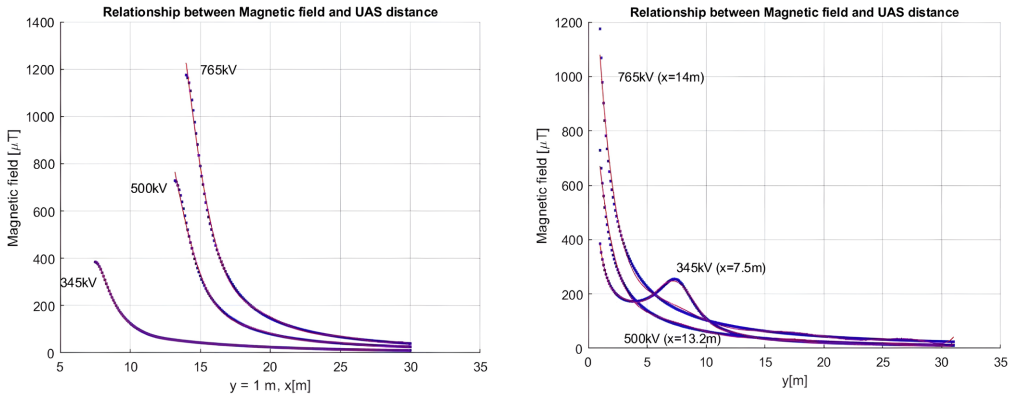

(**a**) (**b**)

Figure 10. Magnetic field distribution around the UAV moving (**a**) horizontally and (**b**) vertically.

Figure 11 shows the magnetic field distribution for horizontal movement above and below the centerline of the three phases or at the centerline of phase B for the double-circuit configuration. The magnetic field reaches its maximum at the horizontal coordinates of the phases and decreases as the UAV moves horizontally and vertically away from the power lines. For example, at y = ±1 m, the magnetic field reaches a maximum of 384 μT, 728 μT, and 1173 μT for the 345 kV, 500 kV, and 765 kV transmission lines, respectively. At y = ±10 m, the magnetic field decreases to 8.9 μT, 59 μT, and 99 μT, respectively.

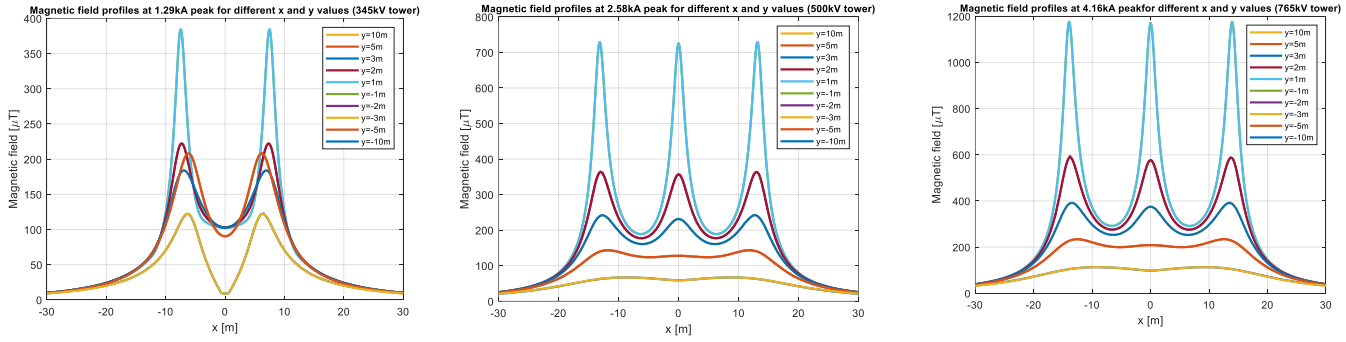

(**a**) (**b**) (**c**)

Figure 11. Lateral profiles of the magnetic field for heights between −10 and +10 m for the three power line voltages: (**a**) 345 kV, (**b**) 500 kV, and (**c**) 765 kV.

Figure 12 depicts the magnetic field for the circular flights around the power lines at four different radius values. Similar to the electric field case, the UAV movement began on the right side of the transmission line (0°) and ended on the left side (180°). For these two angles, the magnetic field values are higher for the 500 kV and 765 kV power lines. For the 345 kV power line, the magnetic field presents two maxima at 40° and 140° and a minimum at approximately 90°. In general, the magnetic field decreases as the radius increases. The highest field values correspond to an approximate radius of 15 m due to the shape of the towers.

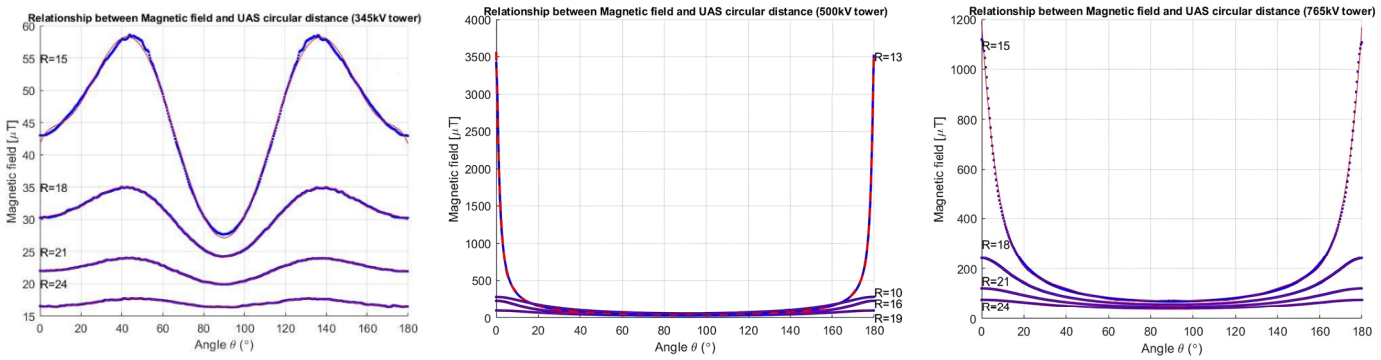

(**a**) (**b**) (**c**)

Figure 12. Magnetic field as a function of angle and radius for the three power line voltages: (**a**) 345 kV, (**b**) 500 kV, and (**c**) 765 kV.

Figure 13 shows a three-dimensional map of the magnetic field intensity. Similar to the electric field case, the magnetic field is concentrated around the phase conductors. As the UAV moves away from the phase conductors, the magnetic field gradually decreases.

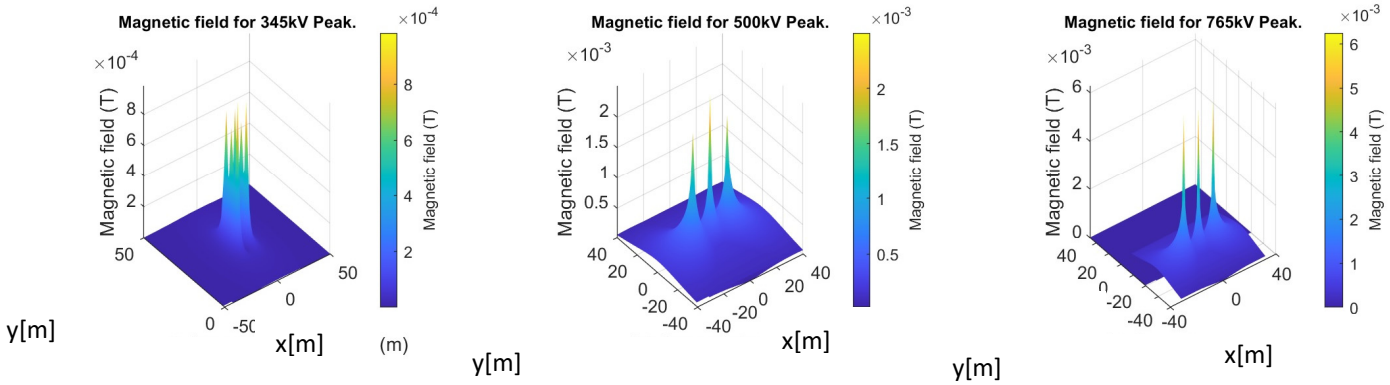

(**a**) (**b**) (**c**)

Figure 13. Three-dimensional plots of the magnetic field intensity for the three power line voltages: (**a**) 345 kV, (**b**) 500 kV, and (**c**) 765 kV.

3.3. Minimum Distance Constraints Analysis for UAV Inspection

Figure 14 illustrates the safe distance as a function of the UAV's electric field strength and magnetic field intensity for the three types of power lines during both horizontal and vertical inspections. The minimum safe distance for a UAV during a power line inspection is also determined by the UAV's ability to resist EMI. This capability is primarily determined by the UAV's design.

Tables 2 and 3 list the computed safe distances for various electric and magnetic field strength values. For example, if the electric field strength of the UAV is 50 kV/m [2], then the minimum safe horizontal and vertical distances (x_s, y_s) would be (0.54 m, 0.6 m), (0.94 m, 1.03 m), and (1.37 m, 1.5 m) for the 345 kV, 500 kV, and 765 kV power lines, respectively. However, if the magnetic field is the determining factor for the minimum safe distance, as mentioned in [2], then a value of 180 µT would result in (1.90 m, 8.76 m), (3.9 m, 3.92 m), and (5.1 m, 6.2 m) as the minimum safe distances from the 345 kV, 500 kV, and 765 kV power lines, respectively.

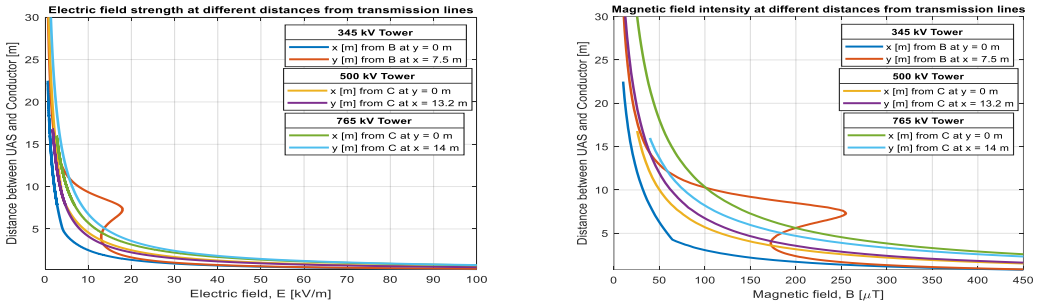

(**a**) (**b**)

Figure 14. Safe distance from power line conductor versus distance for the 345 kV, 500 kV, and 765 kV power line voltages for (**a**) electric field and (**b**) magnetic field.

Table 2. Minimum safe distances for various electric field strengths.

		$(x_s, y_s)(m)$	
Electric Field Strength [kV/m]	**345 kV**	**500 kV**	**765 kV**
10	≥(2.50, 9.35)	≥(4.14, 4.58)	≥(5.74, 6.77)
20	≥(1.35, 1.64)	≥(2.23, 2.49)	≥(3.16, 3.58)
30	≥(0.91, 1.01)	≥(1.53, 1.69)	≥(2.2, 2.42)
40	≥(0.68, 0.75)	≥(1.17, 1.28)	≥(1.69, 1.82)
50	≥(0.54, 0.60)	≥(0.94, 1.03)	≥(1.37, 1.5)
60	≥(0.45, 0.49)	≥(0.79, 0.86)	≥(1.16, 1.22)
70	≥(0.38, 0.42)	≥(0.68, 0.74)	≥(1.0, 1.04)
80	≥(0.33, 0.36)	≥(0.60, 0.64)	≥(0.88, 0.92)
90	≥(0.29, 0.32)	≥(0.53, 0.57)	≥(0.76, 0.81)
100	≥(0.26, 0.29)	≥(0.48, 0.56)	≥(0.71, 0.74)

Table 3. Minimum safe distances for various magnetic field intensities.

		$(x_s, y_s)(m)$	
Magnetic Field Intensity [μT]	**345 kV**	**500 kV**	**765 kV**
100	≥(3.06, 10.28)	≥(6.1, 6.73)	≥(8.2, 10.35)
120	≥(2.65, 9.77)	≥(5.3, 5.73)	≥(7.12, 8.85)
140	≥(2.34, 9.37)	≥(4.71, 4.97)	≥(6.31, 7.74)
160	≥(2.07, 9.05)	≥(4.24, 4.39)	≥(5.65, 6.88)
180	≥(1.90, 8.76)	≥(3.9, 3.92)	≥(5.1, 6.2)
200	≥(1.71, 8.48)	≥(3.56, 3.56)	≥(4.7, 5.6)
220	≥(1.56, 8.19)	≥(3.3, 3.24)	≥(4.34, 5.13)
240	≥(1.44, 7.87)	≥(3, 2.99)	≥(4.03, 4.73)
260	≥(1.34, 1.59)	≥(2.9, 2.77)	≥(3.77, 4.39)
280	≥(1.25, 1.45)	≥(2.74, 2.57)	≥(3.53, 4.09)

3.4. Transient Magnetic Filed

Electrical faults between any of the phases or ground, or between phases, are transient events with durations ranging from 0.08 to 1.0 s, depending on the type and location of the fault [20]. To model the transient magnetic field, an external circuit was created to simulate the current flow through the transmission lines during a phase-to-phase fault

scenario. Figure 15a–c illustrates the circuit configurations for the 345 kV, 500 kV, and 765 kV transmission lines, where the short circuit is introduced between phases A and B.

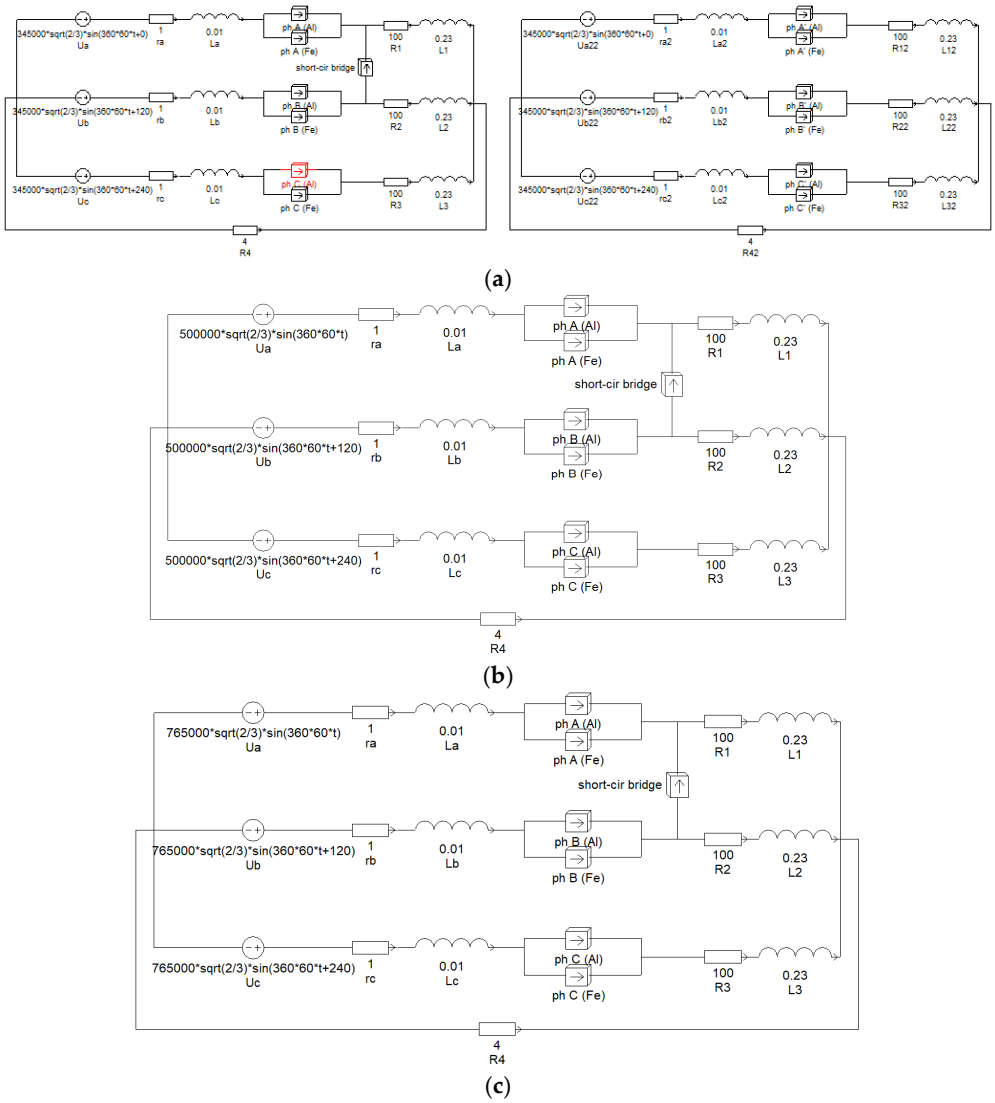

Figure 15. Circuit diagram for modeling transient magnetic field in (**a**) 345 kV transmission line, (**b**) 500 kV transmission line, and (**c**) 765 kV transmission line.

In this study, a 0.1 s simulation had the fault starting at 0.96 s and ending at 1.06 s [11]. Figure 16 shows the short-circuit bridge currents and voltages for 345 kV, 500 kV, and 765 kV transmission lines during the 0.1 s transient period. The short-circuit bridge current peaks at approximately 34 MA, 49 MA, and 70 MA for the respective voltage levels, while the short-circuit bridge voltage peaks at 0.5 MV, 0.7 MV, and 1 MV. The figures reveal that the current and voltage spikes occur significantly faster than the entire 0.1 s duration. The graphs indicate that the main current and voltage transients last approximately 0.02 s.

Figure 17 shows the current and voltage during the simulated phase-to-phase fault in our electrical transmission system. As the fault occurs at the specific time point, Phase A current sharply increases, reaching its peak at 0.99 s. Similarly, Phase B current experiences a rapid rise, peaking at 1.05 s.

Figure 18 depicts the peak magnetic flux density observed across the transmission line at various locations. The plots exhibited the magnetic flux density for different heights above and below the transmission lines. As per the plot, one meter below or above the transmission line, the peak magnetic flux density is 10.5 mT, 15 mT, and 23 mT for the

345 kV, 500 kV, and 765 kV power lines, respectively. At the center of phase B, 10 m above or below the transmission lines, the peak magnetic field density reduces to 0.75 mT, 1 mT, and 1.8 mT for the 345 kV, 500 kV, and 765 kV power lines, respectively. Moreover, the peak magnetic field density values are approximately 26, 20.2, and 20 times higher for the 345 kV, 500 kV, and 765 kV power lines, respectively, compared to the magnetic field density under normal operating conditions. Our results align with the previous research in [21], particularly with measurements taken a few meters above the ground.

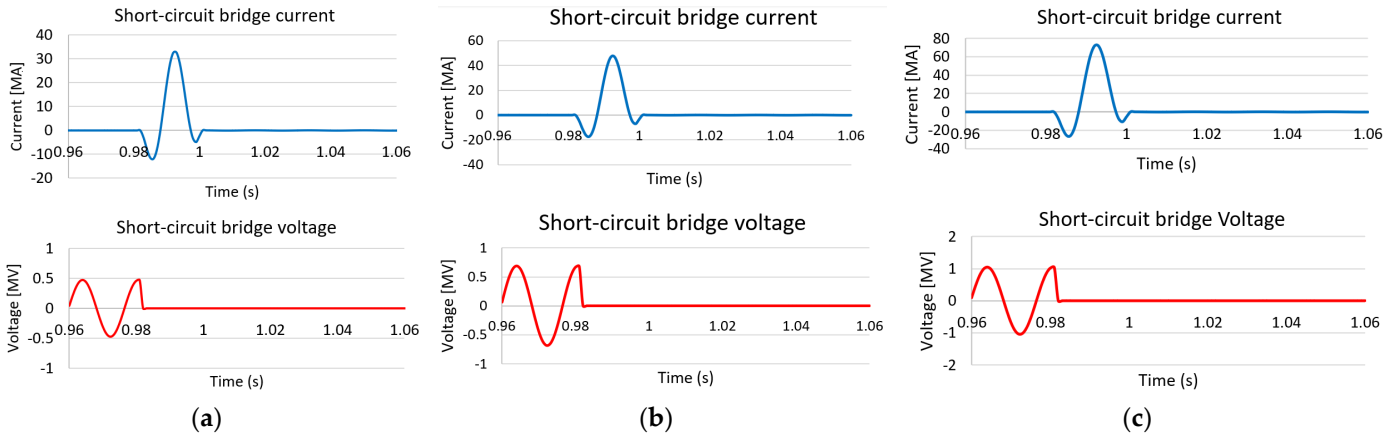

Figure 16. Short-circuit bridge voltages and currents for (**a**) 345 kV transmission line, (**b**) 500 kV transmission line, and (**c**) 765 kV transmission line.

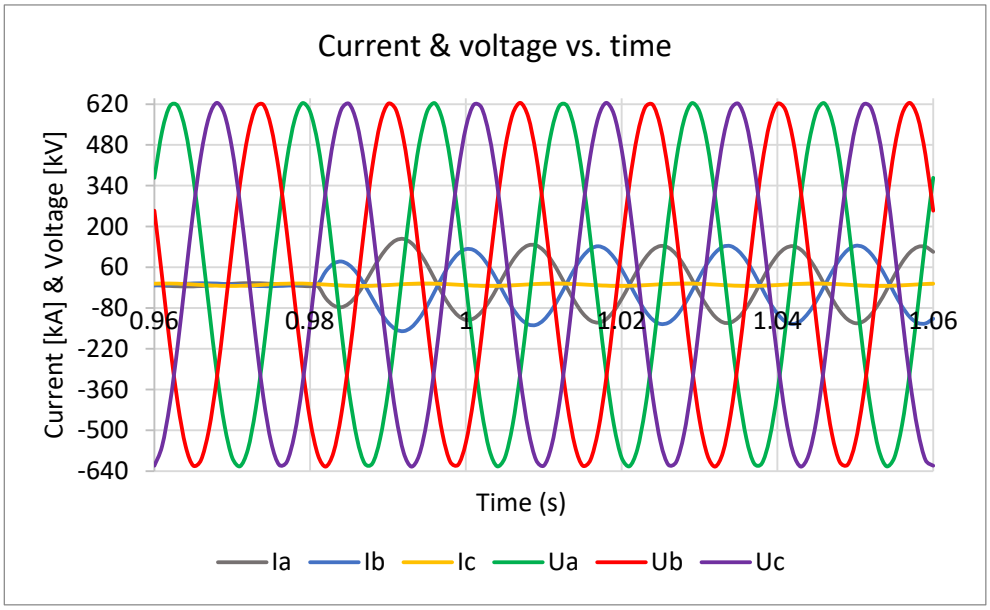

Figure 17. Three-phase voltages and currents during the phase-to-phase fault between phases A and B.

Figure 19 shows a map of the transient magnetic field intensity. The magnetic field is concentrated around the phase-to-phase short circuit and gradually decreases with distance from the fault phase conductors.

The magnetic field intensity at various angles and radii around the transmission line is shown in Figure 20. The data show that the magnetic field decreases as the radius increases. However, the highest magnetic field intensity values are found at a radial distance of 13 m for the 500 kV transmission tower and 15 m for the 765 kV transmission tower. At these distances, the UAV would be right on top of the transmission line conductors, which is why the magnetic field values are very high.

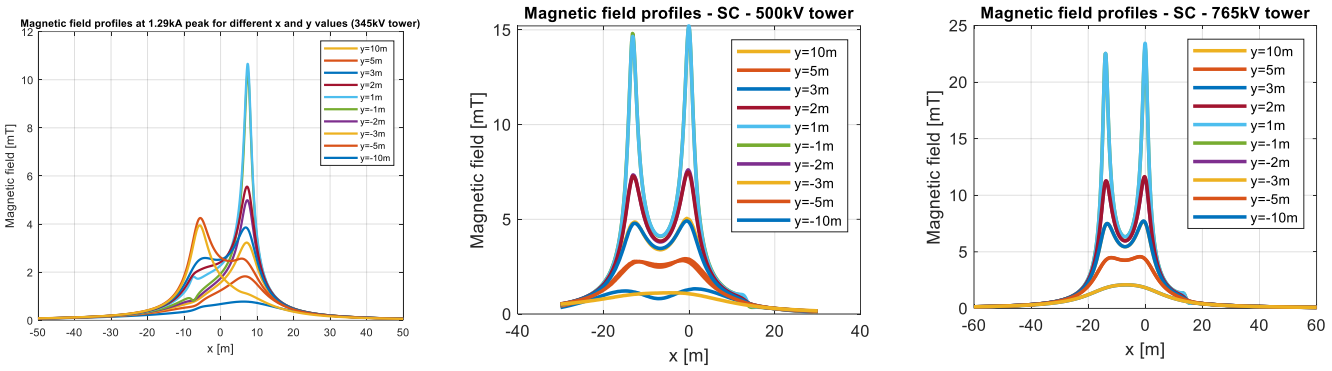

(**a**) (**b**) (**c**)

Figure 18. Peak Values of the EMF at different x and y locations for phase-to-phase short: (**a**) 345 kV; (**b**) 500 kV; and (**c**) 765 kV.

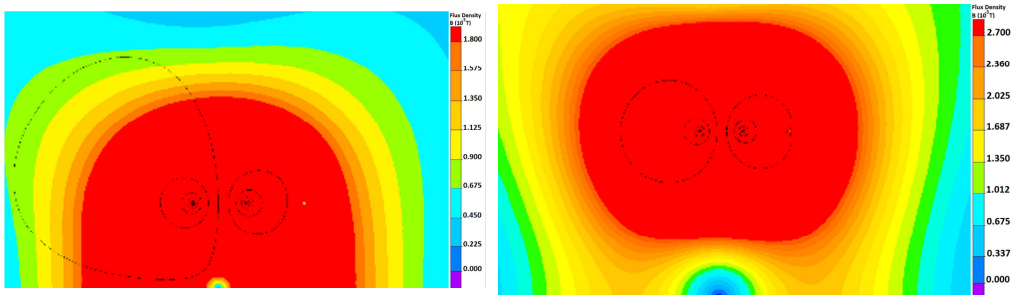

(**a**) (**b**)

Figure 19. Transient magnetic field distribution around (**a**) 500 kV and (**b**) 765 kV.

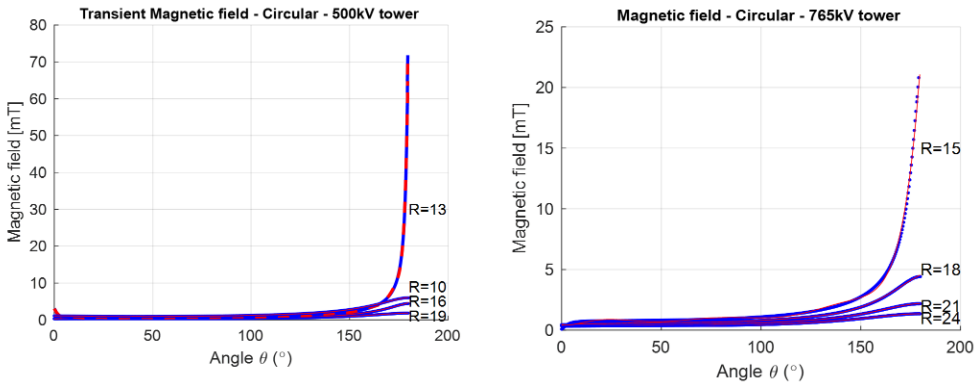

(**a**) (**b**)

Figure 20. Peak values of the magnetic field at four different radii values for (**a**) 500 kV power line and (**b**) 765 kV power line.

As expected, the results show that the magnetic field is high near the transmission line and decreases as the distance from the transmission line increases. The circulation of the short-circuit current bridge produces a high magnetic field of the order of milli Tesla. The maximum amplitude of the magnetic field for a phase A to phase B fault is about 20 and 18 times greater for the 500 kV and 765 kV power lines, respectively, than the nominal value.

Figure 21 illustrates the safe distance as a function of the magnetic field intensity of the UAV for three types of power lines during both horizontal and vertical inspections. By understanding the electric or magnetic field strengths of a UAV, one can determine the minimum safe distance for that UAV from Figure 20. It is worth noting that, in addition to the environment around the transmission lines, the design of the UAV will play a crucial role in

determining the maximum magnetic field strength that the UAV can safely tolerate. Various factors, such as the placement of electronic components, the selection of materials, and the overall shielding strategy, will influence the UAV's susceptibility to magnetic interference.

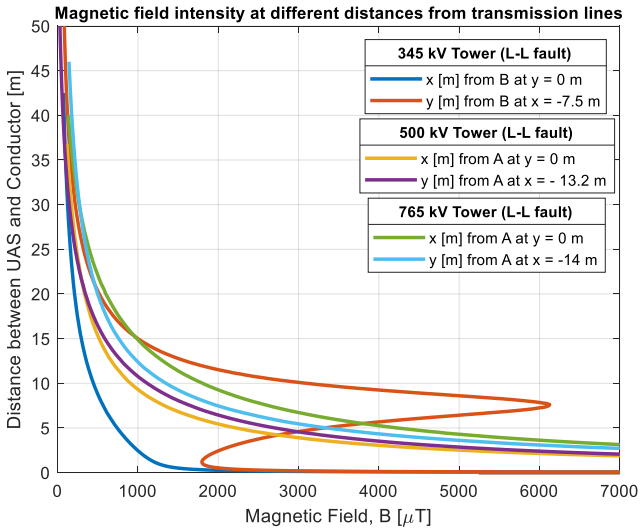

Figure 21. Minimum safe distance as a function of magnetic field strength.

Table 4 lists the computed safe distances for various magnetic field intensity values during phase-to-phase fault. For example, if the magnetic field is the determining factor for the minimum safe distance, as mentioned in [2], then a value of 180 μT would result in minimum safe distances of (22.74 m, 33.11 m), (29.2 m, 27.11 m), and (39.4 m, 35.62 m) from the 345 kV, 500 kV, and 765 kV power lines, respectively.

Table 4. Minimum safe distances for various magnetic field intensities during phase-to-phase fault.

	$(x_s, y_s)(m)$		
Magnetic Field Intensity [μT]	**345 kV**	**500 kV**	**765 kV**
100	≥(34.86, 45)	≥(19.53, 36.01)	≥(25.8, 45.2)
120	≥(30.77, 40.63)	≥(22.11, 32.36)	≥(29.33, 42.15)
140	≥(27.42, 37.57)	≥(24.91, 30.42)	≥(33.01, 39.29)
160	≥(24.87, 35.03)	≥(27.21, 28.76)	≥(36.33, 37.29)
180	≥(22.74, 33.11)	≥(29.2, 27.11)	≥(39.4, 35.62)
200	≥(20.91, 36.01)	≥(30.93, 31.47)	≥(42.08, 34.09)
220	≥(19.3, 30)	≥(32.42, 24.95)	≥(44.28, 32.8)
240	≥(17.91, 28.76)	≥(33.76, 23.97)	≥(46.22, 31.54)
260	≥(16.78, 27.68)	≥(34.91, 23.06)	≥(47.9, 30.45)
280	≥(15.7, 26.71)	≥(35.95, 22.26)	≥(49.34, 29.43)

3.5. Validations of the Results

This study develops comprehensive guidelines for pre-flight planning and operational decision making in UAV operations. Tables 2 and 3 offer baseline guidance for maintaining safe operational distances under normal conditions, while Table 4 is for scenarios that involve line fault. Thus, the directives in Table 4 serve as a precautionary framework, empowering UAV operators with the requisite knowledge to maintain safe distances in the face of unforeseen line faults. This is particularly pertinent in areas that have recently experienced severe weather, for example, which can increase the likelihood of faults. In addition, regions of the transmission lines located further from the circuit breaker are

especially vulnerable, as a phase-to-phase fault could inflict significant damage on nearby UAVs. Operators should also have access to data from the electricity provider and be mindful of the surrounding vegetation, as it can signal the potential for branches or entire trees to fall onto the lines and induce phase-to-phase faults. In this case, the UAV will switch to a fault-mode flight path. Furthermore, our study advocates a two-pronged approach to integrating these guidelines into UAV operational protocols. With direct collaboration with power authorities and knowledge of local conditions and nuances, flight crews can incorporate these guidelines into pre-flight planning. This planning process should encompass a variety of considerations, including the probability of line faults, informed by the historical and current state of the transmission lines. Conversely, a more conservative stance is advised for operators like contractors who might not have in-depth knowledge of the specific electromagnetic fields and the implications of the field effects associated with the transmission lines they are inspecting. Such an approach would involve adhering to the guidelines to determine minimum safe distances based on worst-case scenarios, thereby providing a substantial margin of safety.

The Quickfield simulation results were verified using EMFACDC. This user-interactive tool is based on analytical methods [22] to produce precise profiles of the electric field and lateral magnetic field at any height above ground level that the user specifies. The results obtained from the two methods were in excellent agreement, as shown in Figure 22, which compares the lateral profile of the electric field for the two methods at 1 m above the conductors for the three types of power lines. Additionally, the findings from this study align with those of previously published research, including the calculations and measurements for distances of a few meters above ground [21].

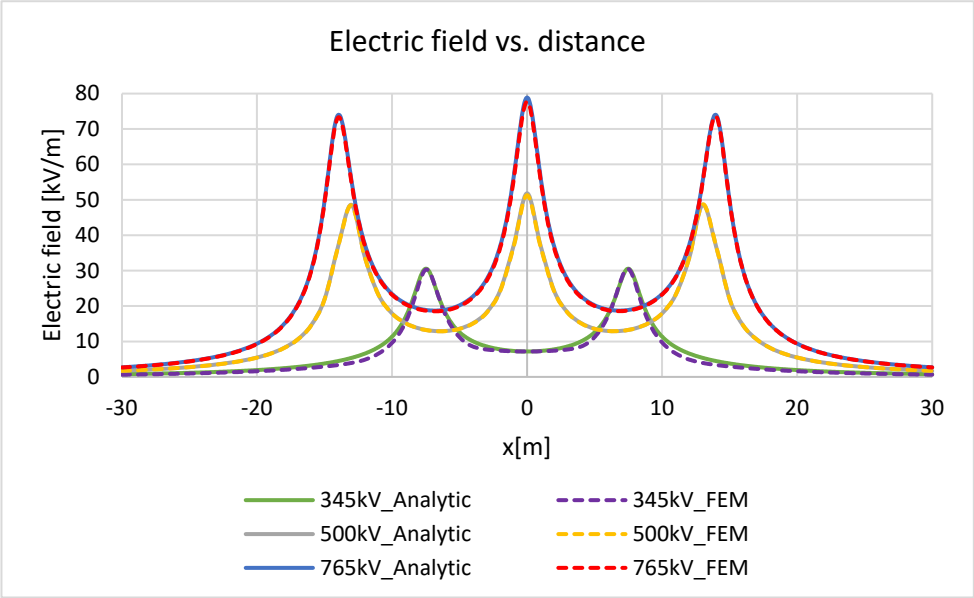

Figure 22. Comparison of lateral profiles of the electric field obtained using analytical methods and FEM for 345 kV, 500 kV, and 765 kV power lines.

Figure 23 displays the error in the lateral electric field profile at a height of 1 m above the conductors between the FEM and the analytical method for power lines of 345 kV, 500 kV, and 765 kV. The difference in the electric measurements between the two methods fluctuates with distance. However, the percentage of error remains minimal, ranging from only 0% to 2.5%, depending on the proximity to the power lines.

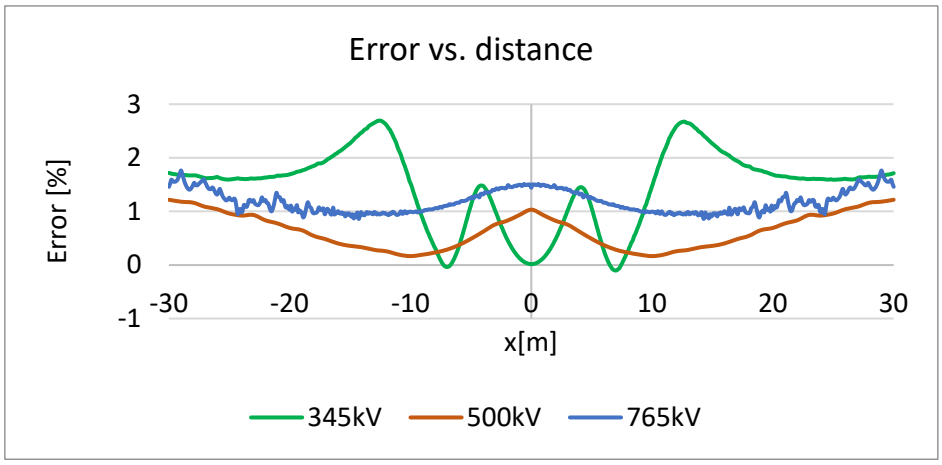

Figure 23. Comparison of electric field errors using FEM and analytical methods for 345 kV, 500 kV, and 765 kV power lines.

4. Conclusions

We used the QuickField software to compute and analyze the distribution of the electric and magnetic field profiles produced by EHV transmission lines (345 kV, 500 kV, and 765 kV) from the perspective of UAV exposure. The results were compared to those obtained from other software based on analytical methods. The two simulations demonstrated excellent agreement. Tables 2 and 3 provide guidance for operations around transmission lines, giving the horizontal and vertical distances for the three power transmission levels, given the field profiles. If a line fault is expected during the inspection, then Table 4 can be used as a guide. This study shows that a phase-to-phase short circuit can cause a significant increase in the strength of the magnetic field surrounding a transmission line. This increase can be as much as more than eighteen times the normal magnetic field strength. As a result, the safe distance for a UAV from a transmission line during a short circuit is much greater than the safe distance under normal operating conditions. One approach is to assume a level of local awareness and expertise that a UAV flight crew might be expected to have if working directly with a power authority over the transmission lines in question. These distances would be integrated into the pre-flight planning for an operation, given the normal information required to conduct a safe flight, including ambient weather and forecasts. On the other hand, it may be best to abstract these results into conservative assumptions and minimum safe distances suitable for an operator, such as a contractor less familiar with the EMFs and field effects in question. Overall, minimum safe distances should likely be calculated as a single, conservative value for a given operation and a given transmission line's characteristics.

The next phase of this research will focus on analyzing the impact of electric and magnetic fields on the various subsystems and components of a UAV, including the GPS receiver, inertial measurement unit, light detection and ranging (LIDAR), speed controllers, and motors.

Author Contributions: Conceptualization, I.B.; methodology, I.B.; software, I.B.; validation, I.B.; formal analysis, I.B.; investigation, I.B.; data curation, I.B.; writing—original draft preparation, I.B. and N.K.; writing—review and editing, I.B. and N.K.; visualization, I.B.; supervision, N.K.; project administration, N.K.; funding acquisition, N.K. All authors have read and agreed to the published version of the manuscript.

Funding: This research was funded by the Federal Aviation Administration (FAA), Award Number A45_A11L.UAS.87.

Data Availability Statement: Data are contained within the article.

Acknowledgments: The authors would like to express their gratitude to the Federal Aviation Administration (FAA) for their support of the project titled "Shielded UAS Operations: Detect and Avoid (DAA)." The content of this paper is the sole responsibility of the authors and does not necessarily reflect the official views or policies of the FAA.

Conflicts of Interest: The authors declare no conflicts of interest.

References

1. Kim, S.-G.; Lee, E.; Hong, I.-P.; Yook, J.-G. Review of Intentional Electromagnetic Interference on UAV Sensor Modules and Experimental Study. *Sensors* **2022**, *22*, 2384. [CrossRef] [PubMed]
2. Zhang, W.; Ning, Y.; Suo, C. A Method Based on Multi-Sensor Data Fusion for UAV Safety Distance Diagnosis. *Electronics* **2019**, *8*, 1467. [CrossRef]
3. National Coordinating Center for Communications (NCC). *Electromagnetic Pulse (EMP) Protection and Resilience Guidelines for Critical Infrastructure and Equipment*; Version 2.2; National Cybersecurity and Communications Integration Center: Arlington, VA, USA, 2019.
4. Lusk, R.M.; Monday, W.H. *An Early Survey of Best Practices for the Use of Small Unmanned Aerial Systems by the Electric Utility Industry*; Oak Ridge National Laboratory: Oak Ridge, TN, USA, 2017.
5. Chen, D.-Q.; Guo, X.-H.; Huang, P.; Li, F.-H. Safety Distance Analysis of 500 kV Transmission Line Tower UAV Patrol Inspection. *IEEE Lett. Electromagn. Compat. Pract. Appl.* **2020**, *2*, 124–128. [CrossRef]
6. Park, J.; Kim, S.; Lee, J.; Ham, J.; Oh, K. Method of operating a GIS-based autopilot drone to inspect ultrahigh voltage power lines and its field tests. *J. Field Robot.* **2020**, *37*, 345–361. [CrossRef]
7. Silva, M.F.; Honório, L.M.; Santos, M.F.; Vidal, V.F.; Mercorelli, P. Model and Validation of the Electromagnetic Interference Produced by Power Transmission Lines in Robotic Systems. In Proceedings of the 2021 25th International Conference on System Theory, Control and Computing (ICSTCC), Iasi, Romania, 20–23 October 2021; pp. 266–271.
8. da Silva, M.F.; Honório, L.M.; Marcato, A.L.; Vidal, V.F.; Santos, M.F. Unmanned aerial vehicle for transmission line inspection using an extended kalman filter with colored electromagnetic interference. *ISA Trans.* **2020**, *100*, 322–333. [CrossRef] [PubMed]
9. Virjoghe, E.O.; Nescu, D.E.; Stan, M.F.; Cobianu, C. Numerical determination of electric field around a high voltage electrical overhead line. *J. Sci. Arts* **2012**, *4*, 487–496.
10. Boukabou, I.; Foust, L.; Benouadah, S.; Rupanetti, D.; Wolf, J.; Kaabouch, N. Electric Field Around Extra-High Voltage Transmission Lines for UAS Powerline Inspection. In Proceedings of the 2022 North American Power Symposium (NAPS), Salt Lake City, UT, USA, 9–11 October 2022; pp. 1–6. [CrossRef]
11. Foust, L.; Boukabou, I.; Rupanetti, D.; Benoudah, S.; Kaabouch, N. UAS Safe Distance due to Magnetic Field of Extra High Voltage Transmission Lines during a Phase-to-Phase Short Circuit. In Proceedings of the 2022 North American Power Symposium (NAPS), Salt Lake City, UT, USA, 9–11 October 2022; pp. 1–5. [CrossRef]
12. Brown, J. *Great Northern Transmission Line Project–EMF and Corona Effects Calculations from Appendix I, Memorandum to L. Henriksen*; Portland, OR, USA, 2013.
13. Stangeland, K. Positioning in Electromagnetic Fields. Master's Thesis, University of Stavanger, Stavanger, Norway, 2015.
14. Anderson, J.G. *Transmission Line Reference Book: 345 kV and Above*; Electric Power Research Institute: Palo Alto, CA, USA, 1982.
15. Switch Gear and Substations, Siemens Energy Sector. *Power Engineering Guide*, 8th ed.; Erlangen, Germany, 2017.
16. Lunca, E.C.; Neagu, B.C.; Vornicu, S. Finite Element Analysis of Electromagnetic Fields Emitted by Overhead High-Voltage Power Lines. In *Numerical Methods for Energy Applications*; Power Systems; Springer International Publishing: Berlin/Heidelberg, Germany, 2021; ISBN 978-3-030-62190-2.
17. Faiz, J.; Ojaghi, M. Instructive Review of Computation of Electric Fields using Different Numerical Techniques. *Int. J. Eng. Educ.* **2002**, *18*, 344–356.
18. Tera Analysis Ltd. *QuickField Finite Element Analysis System*; Version 6.3.1 User's Guide; Tera Analysis Ltd.: Svendborg, Denmark, 2018.
19. Nigbor, R.J.; Pakala, W.E. A Survey of Methods for Calculating Transmission Line Conductor Surface Voltage Gradients. *IEEE Trans. Power Appar. Syst.* **1996**, *PAS-98*, 1996–2014.
20. Finneran, S.; Krebs, B.; Bensman, L. *Criteria for Pipelines Co-Existing with Electric Power Lines*; The INGAA Foundation: Washington, DC, USA, 2015; Volume 4.
21. Ayad, A.; Krika, W.; Boudjella, H.; Benhamida, F.; Horch, A. Simulation of the electromagnetic field in the vicinity of the overhead power transmission line. *Eur. J. Electr. Eng.* **2019**, *21*, 49–53. [CrossRef]
22. Fikry, A.; Lim, S.C.; Ab Kadir, M.Z.A. EMI radiation of power transmission lines in Malaysia. *F1000Research* **2021**, *10*, 1136. [CrossRef] [PubMed]